

Convection in Scaled Turbine Internal Cooling Passages With Additive Manufacturing Roughness

Gabriel J. Stafford

Department of Mechanical Engineering,
Baylor University,
Waco, TX 76798-7356
e-mail: gstafford@jasc-controls.com

Stephen T. McClain¹

Department of Mechanical Engineering,
Baylor University,
Waco, TX 76798-7356
e-mail: stephen_mcclain@baylor.edu

David R. Hanson

Applied Research Laboratory,
The Pennsylvania State University,
University Park, PA 16802
e-mail: drh5013@psu.edu

Robert F. Kunz

Department of Mechanical Engineering,
The Pennsylvania State University,
University Park, PA 16802
e-mail: rfk102@psu.edu

Karen A. Thole

Department of Mechanical Engineering,
The Pennsylvania State University,
University Park, PA 16802
e-mail: kthole@psu.edu

Additive manufacturing processes, such as direct metal laser sintering (DMLS), enable the creation of novel turbine cooling internal passages and systems. However, the DMLS method produces a significant and unique surface roughness. Previous work in scaled passages analyzed pressure losses and friction factors associated with the rough surfaces, as well as investigated the velocity profiles and turbulent flow characteristics within the passage. In this study, the heat transfer characteristics of scaled additively manufactured surfaces were measured using infrared (IR) thermography. Roughness panels were CNC machined from plates of aluminum 6061 to create near isothermal roughness elements when heated. Fluid resistance differences between the aluminum roughness panels and roughness panels constructed from ABS plastic using the same roughness patterns from McClain et al. (2020, "Flow in a Simulated Turbine Blade Cooling Channel With Spatially Varying Roughness Caused by Additive Manufacturing Orientation," ASME Turbo Expo 2020, Turbomachinery Technical Conference and Exposition, Virtual Conference, Sept. 21–25, GT2020-16069) were investigated. Finally, the overall thermal performance enhancements and friction losses were assessed through the calculation of surface averaged "global thermal performance" ratios. The global thermal performance characterizations indicate results in-line with those found for traditional commercial roughness and slightly below traditional internal passage convection enhancement methods such as swirl chambers, dimples, and ribs. The passages investigated in this study do not include compressibility effects or the long-wavelength artifacts and channel geometric deviations observed by Wildgoose et al. (2020, "Impact of Additive Manufacturing on Internal Cooling Channels with Varying Diameters and Build Directions," ASME Turbo Expo 2020, Turbomachinery Technical Conference and Exposition, Virtual Conference, Sept. 21–25, GT2020-15049). However, the results of this study indicate that, based on the roughness augmentation alone, artificial convective cooling enhancers such as turbulators or dimples may still be required for additively manufactured turbine component cooling.

[DOI: 10.1115/1.4052524]

Keywords: fluid dynamics and heat transfer phenomena in compressor and turbine components of gas turbine engines, heat transfer

Introduction

Additive manufacturing (AM) technologies enable the creation of parts with geometries more complex than those possible using more traditional subtractive manufacturing technologies. Because of the novel geometries allowed, AM is being explored for the potential to improve the design and manufacturing of gas turbine blades and components.

Maximizing the initial cost-effectiveness of a gas turbine system requires maximizing the turbine inlet temperature of the combustion products exiting the combustor, with current technology allowing for temperatures in excess of 1500 °C [1]. However, these temperatures are close to the melting temperature for the metals which make up the blades. Thus, the performance of the turbine blades under extreme heat becomes a major limiting factor in engine design and effectiveness.

To maintain blade integrity during high-temperature operation, cooler air from the compressor is directed through small interior

cooling passages manufactured within each individual blade. These passages provide increased heat transfer away from the blade and thus serve to maintain the life and maximize the efficiency of the engine. AM has the potential to improve turbine blade cooling by enabling the manufacture of complex cooling passages in situ. Thus, AM would reduce the need for the complex cores and core removal process required for cooling passage creation when turbine blades are constructed using metal casting.

The AM process most commonly used to manufacture turbine components is known as direct metal laser sintering (DMLS). DMLS involves the use of a laser to systematically melt layers of fine metal powder, thereby creating the complex geometries of the part. However, the process is known to produce a unique form of roughness on the surface of the AM part [2]. Generally, this roughness could be corrected with post-processing of the surface, but due to the in situ manufacturing and placement of the passages, little can be done to improve the interior surface quality. Additionally, the roughness produced during DMLS varies with the build orientation of the part because of gravitational effects on the heat-affected zone or melt area of the metal powder [2].

Previous work in this space has shown the potential for significant design and performance improvements. Kirsch and Thole [3] additively manufactured wavy microchannels of varying

¹Corresponding author.

Contributed by the International Gas Turbine Institute (IGTI) of ASME for publication in the JOURNAL OF TURBOMACHINERY. Manuscript received July 28, 2021; final manuscript received September 15, 2021; published online November 10, 2021. Tech. Editor: David G. Bogard.

wavelength at the engine component scale in an exploration of potential design improvements to cooling channel design. The work showed performance enhancement related to heat transfer for longer wavelength channels and shed light on the vast design space available with DMLS. Stimpson et al. [4,5] studied AM tolerances and performance, again at the engine scale, using ten test coupons made of CoCr and Inconel 718 at various build orientations. The study presents roughness comparisons between build orientations and proposes new Nusselt number correlations based on experimental heat transfer results.

Hanson et al. [6] furthered the study by scaling roughness geometries by 102x and performing friction and velocity measurements within a custom wind tunnel designed to simulate cooling channel flow. Tests were also completed using an analog roughness made up of randomly placed ellipsoids which were generated to match the roughness statistics of the real surface. The scale of the surface roughness being at wind tunnel size allowed for more detailed flow measurements and served to justify the frictional correlations of Stimpson et al. [5]. McClain et al. [7] presented additional wind tunnel scale measurements of friction and velocity using surface roughnesses that had been created with AM with different build orientations. The work provides detailed frictional and flow measurements for a variety of AM roughness ceiling and floor combinations using hot-film anemometry.

While previous works have provided both friction and heat transfer measurements using AM coupons at the engine component scale [3–5] and efforts have been made to produce detailed friction and velocity measurements at the wind tunnel scale by Hanson et al. [6] and McClain et al. [7], no work has yet been done to provide detailed heat transfer measurements of AM surface roughness at the wind tunnel scale. This study aims to produce those heat transfer measurements, which are essential to the understanding of the thermal performance of spatially varying AM roughness, as well as to characterize the frictional losses and heat transfer enhancement provided by the AM roughness.

To better measure the frictional and heat transfer effects of the surface roughness within a turbine blade cooling air passage, a test channel was constructed with both channel dimensions and roughness elements scaled up to improve measurement quality. One smooth surface and three rough surfaces were created from aluminum plates. The roughness geometries were created using high-fidelity computed tomography (CT) scans or structured light scans as described by McClain et al. [7]. The rough aluminum test plates were used to perform two distinct experiments: (1) friction factor measurements were taken of each surface at Reynolds number intervals of 10,000 using hotwire anemometry and (2) convection coefficients and resulting Nusselt numbers were measured at the same Reynolds number intervals using infrared surface images and steady-state heat transfer approaches.

The measurements were made with the goal of calculating the “Reynolds analogy performance parameter” and “global thermal performance parameter” used by Ligrani [8]. The performance parameters served as useful metrics for quantifying the increase in convective heat transfer relative to the increase in friction factor. The performance parameters may additionally be used to provide a more direct comparison between the thermal performance and frictional cost associated with AM roughness and those associated with the current forms of convection enhancement currently used on the interior of gas-turbine blades such as rib turbulators, surface dimples, or pin fins.

Methodology

In the following sections, the facilities and methods used to achieve the experimental objectives are described. The data reduction and the uncertainty assessment approaches are also presented.

Roughness Internal Flow Tunnel. The roughness internal flow tunnel (RIFT) is an internal flow rig housed at Baylor University,

which was constructed to simulate the flow within an interior cooling passage of a gas turbine blade. The body of the tunnel is made almost entirely of printed ABS plastic and has a highly modular design, with a cross section measuring 228.6 mm by 35.56 mm (9 in. by 1.42 in.), which gives the tunnel a hydraulic diameter of 62.3 mm (2.45 in.). The RIFT has a settling region of 506-mm ($L_s/D_h = 11.2$) and a test section measuring 914 mm (36 in.) in length. Previous efforts to study friction effects and turbulent flow characteristics within the tunnel involved the use of additively manufactured ABS plastic surfaces as the floor and ceiling of the test section [6,7]. Back and side views of the RIFT test section are presented in Fig. 1, and more details regarding the RIFT may be found in Refs. [6,7].

Heat Transfer Test Plate. For this investigation, a heated test stand was constructed by machining a 12.7-mm (0.5-in.) deep by 228.6-mm (9-in.) wide inset channel from a 304.8-mm (12-in.) by 457.2-mm (18-in.) acrylic plate with a thickness of 34.93 mm (1.375 in.). A second inset was cut from the acrylic to form space for heating elements. Spanwise channels were then cut using a 1/8-in. ball mill to form 1.59-mm deep channels where thermocouples were installed to determine the conduction losses through the acrylic base. E-type thermocouples were installed in the channels with butt-welded beads placed at the center span of the acrylic base. Top and isometric views of the acrylic base section are shown in Fig. 2. As depicted in Fig. 1, the heated test is placed such that the heated region is the last 457.2 mm (18 in.) of the length of the RIFT test section.

Inside the heater inset, a layer of neoprene was attached to the acrylic, and two 8” by 8” Omega Polyimide insulated flexible resistance heaters were attached to the top of the neoprene layer to heat the test surfaces. The heaters were powered by two BK-Precision 9104 variable DC power supplies, which were manually set before each test. On the top of the heaters, a sheet of 0.31-mm steel shim was added to maintain thermal contact and evenly distribute energy to the test plate. Finally, the test plates were constructed from aluminum 6061 plate and were machined such that the mean

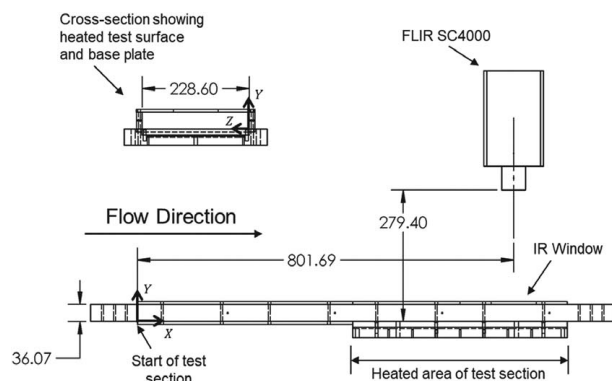


Fig. 1 Back and right views of RIFT showing heater and IR camera positions

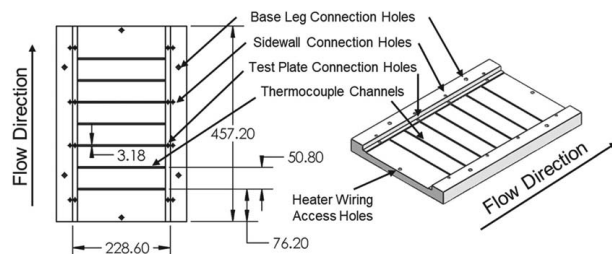


Fig. 2 Heated section acrylic base detail

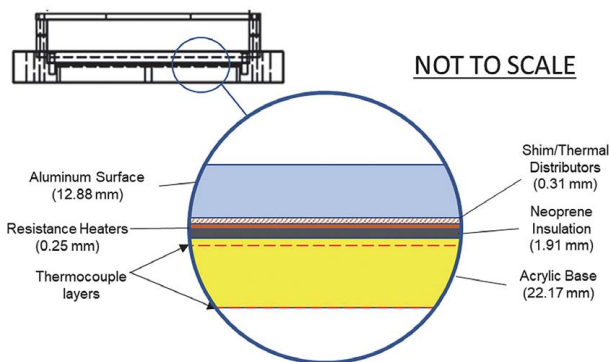


Fig. 3 Test section heater cut-away

thickness was 12.7 mm (0.5 in.). A cut-away of the heated test section is presented in Fig. 3. As noted in Fig. 3, an additional set of thermocouples was attached to the bottom of the test plate directly below the internal thermocouple channels to determine the conduction losses through the acrylic base.

Rough Surfaces. The surfaces used in the investigation have been described in the prior investigations of Hansen et al. [6] and McClain et al. [7]. The rough surfaces were created by scaling either X-ray tomography scans or structured light scans of the internal passages of direct-metal laser sintering (DMLS) coupons constructed in the START Lab at Pennsylvania State University [2]. The coupons were printed with the passages making a 45-deg angle to the build plane. Two of the surfaces came from an Inconel 718 coupon, and the other came from a Hastelloy coupon. Scaling values of 50 \times and 102 \times were chosen to provide a geometric progression ($\times 2.5$) of roughness characteristics.

The surfaces investigated in this study are referred to as the Inco718_Upskin, the Inco718_Downskin, and the Real_x102 surface. Figure 4 presents a top view of the solid-model topography of each rough surface.

Table 1 presents the summary of characteristics for the surfaces as measured from the geometry file used to create each surface. In Table 1, the arithmetic mean roughness, R_a , the root-mean-square roughness, R_q , and the skewness, Skw , are calculated using Eqs. (1)–(3).

$$R_a = \left[\frac{1}{N_p} \sum_{i=1}^{N_p} |Y'| \right] \quad (1)$$

$$R_q = \left[\frac{1}{N_p} \sum_{i=1}^{N_p} (Y'^2) \right]^{1/2} \quad (2)$$

$$Skw = \frac{1}{R_q^3} \left[\frac{1}{N_p} \sum_{i=1}^{N_p} (Y'^3) \right] \quad (3)$$

In Eqs. (1)–(3), $Y' = Y - \bar{Y}$, and \bar{Y} is the mean surface elevation as calculated using Eq. (4).

$$\bar{Y} = \frac{1}{N_p} \sum_{i=1}^{N_p} Y \quad (4)$$

In addition to the statistical descriptions of the surfaces, Table 1 includes estimates of the equivalent sand grain roughness using two correlations. The first correlation estimate is based on the RMS roughness and skewness and is from Flack and Schultz [9].

$$k_{s,F1} = 4.43 R_q (1 + Skw)^{1.37} \quad (5)$$

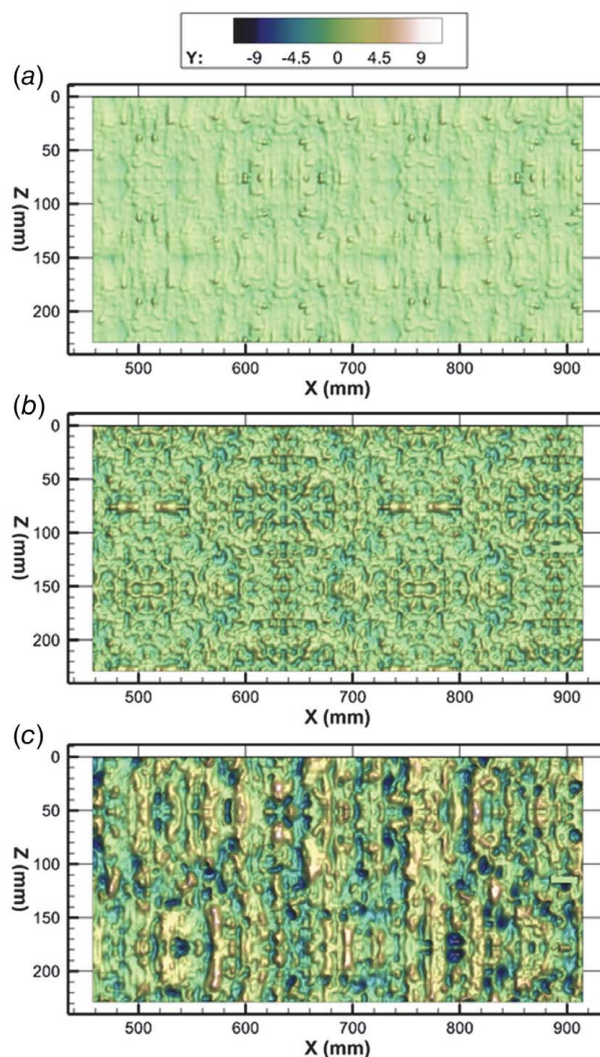


Fig. 4 Top view of heated scaled rough surface sections: (a) Inco718_Upskin, (b) Inco718_Downskin, and (c) Real_x102

The second correlation is from Stimpson et al. [5] and is based on the arithmetic mean roughness.

$$\frac{k_{s,ST}}{D_h} = 18 \frac{R_a}{D_h} - 0.05 \quad (6)$$

The geometry files used to create the surfaces investigated in McClain et al. [7] were used to create the aluminum heat transfer

Table 1 Roughness properties of scaled additively manufactured surfaces

Roughness property	Inco718 Upskin	Inco718 Downskin	Real_x102
Abbreviation	“Up”	“Down”	“Real”
R_a (mm)	0.303	0.737	1.887
R_q (mm)	0.386	0.936	2.436
$k_{s,FS}$ (mm)	2.182	4.623	6.933
$k_{s,ST}$ (mm)	4.179	12.00	30.85
Skw	0.195	0.082	−0.276
R_q/D_h	0.0062	0.0150	0.0391
$k_{s,FS}/D_h$	0.0350	0.0742	0.1113
$k_{s,ST}/D_h$	0.0671	0.1927	0.4951
\bar{y}	0.53	0.65	0.75
D_m (mm)	65.51	77.82	87.50
$\tau_R/\bar{\tau}$	0.904	1.636	1.925

surfaces using a CNC milling machine. Two passes using a 1/4-in. ball mill. Two more finishing passes were made using a 1/8-in. ball mill. Following machining, the plates were painted using a self-etching primer and a flat-black paint to create a surface emissivity of 0.975.

Because of the size of the heat transfer area and the size of the roughness elements investigated, comparing the heat transfer surface coupon roughness to the solid model characterizations of Table 1 presents challenges. Most profilometry systems are intended to measure much smaller roughness than employed in this study, especially for the Real_x102 surface which has a peak-to-valley maximum of 1.84 cm (0.72 in.). Additionally, laser scanner systems that can conceivably characterize that size roughness are not typically certified for roughness measurements following the ISO 4287:1997 standard.

To provide an example comparison of the machined surface to the computational model, a Keyence VR-3100 wide-area structured-light profilometry system with a height measurement range of ± 5 mm was used to measure a 24 mm by 18 mm (0.95 in. by 0.71 in.) area of the Inco718_Downskin surface. Figure 5 presents a comparison of the solid model geometry used to create the measured Inco718_Downskin aluminum surface. Figure 5 demonstrates the CNC machining process results in a surface that generally represents the solid model, but tool marks are clearly visible on the surface.

Table 2 presents a comparison of the roughness statistics for the model surface section and the measured aluminum surface. Generally, the peak-to-valley and root-mean-square roughness are within 6% of the model, but the skewness of the aluminum surface is 10.4% higher than the skewness for the surface computational model.

Surface Temperature Measurements. A FLIR SC4000 infrared camera supported 279.4-mm (11-in.) above the test section was used to measure the surface temperature of the rough aluminum test plates. Figure 1 depicts the position of the IR camera above the test section. The IR camera was allowed to view the surface downward through an IR viewing window set in the ceiling of the tunnel. The FLIR SC4000 has an indium-antimonide (InSb) detector and resolution of 320 by 256 pixels. A 25-mm lens is used producing an imaged area of 10.72 cm by 8.58 cm at the distance of 27.94 cm from the mean test surface. The camera was placed with the infrared chip parallel to the test surface, and a 76-mm (3-in.) “C-Range” circular infrared window was installed in the RIFT ceiling panel. A 0.76-mm (0.030-in.) lip was CNC machined out of an aluminum ceiling panel to hold the IR window in place during testing.

During testing, the infrared camera captured 100 frames of temperature measurements at 30 frames per second. Since the IR window was circular and the IR images captured a larger

Table 2 Comparison of computational and measured features for the Inco718_Downskin surface

Property	Model	Aluminum
N_p	768	785,788
R_{PV} (mm)	5.1994	4.9693
R_q (mm)	1.0465	0.9889
Sk_w	0.2393	0.2645

rectangular area, the IR images included temperature features that were not from the heat transfer surface. A MATLAB code was created which generated a mask for use with the IR surface images. The surface mask served to isolate only the portion of the images which gave relevant temperature data by disregarding certain portions of each image. The masked-out regions included the ceiling of the tunnel in which the IR viewing window was set, as well as a reflection of the IR sensor off of the viewing window, which was visible in the center of every surface image.

The percentage of pixels masked in the infrared images changes slightly from case to case because of slight changes in the camera location following the changing of the surface panels. However, for a typical case, 4.77% (3905 pixels) are masked for the center reflection, and 44.5% (36,455 pixels) are masked for the ceiling of the tunnel. Thus, approximately 50.73% of the infrared image pixels were used for the convection calculations. Complete details of the masking and infrared image reduction process may be found in Stafford [10].

Convection Measurements. Prior to each heat transfer measurement in the RIFT, the apparatus was left at least 24 h to reach thermal equilibrium. To begin each measurement, an in situ scheme was used to calibrate all of the plate thermocouple and thermistor measurements to the mean infrared temperature, defined using Eq. (7). The reference temperature was defined to be the average temperature of the unmasked region of the surface image at the time of calibration. The reference temperature was then used in conjunction with a calibration data set to determine a calibrated temperature for each temperature measurement using Eq. (8). Only calibrated temperatures were used in the data reduction and analysis.

$$T_{ref} = \text{mean}(T_{im,cal}) \quad (7)$$

$$T_{run} = T_m - (T_{cal} - T_{ref}) \quad (8)$$

Following temperature calibration, the power supplies for all other instrumentation were turned on, and the remaining sensors were allowed to warm up for approximately 30 min. During this

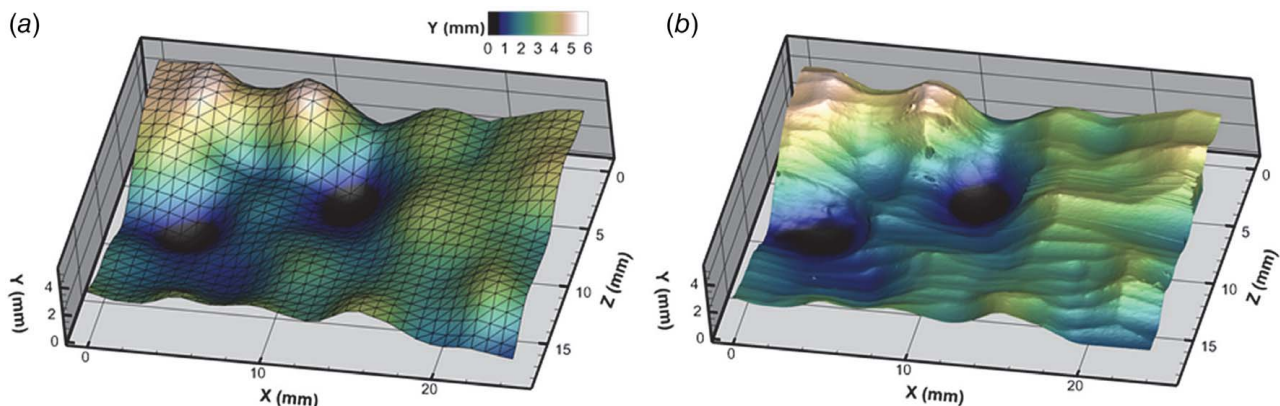


Fig. 5 Demonstration of geometry differences: (a) computational model geometry and (b) measured aluminum surface

time, a LABVIEW program was started to monitor and log the tunnel's Reynolds number, flowrate, pressure, as well as all relevant tunnel temperatures and room conditions.

Using a variable autotransformer, the desired Reynolds number of the flow was then set. Test Reynolds numbers ranged from 10,000 to 70,000 in increments of 10,000. Because of fan performance limitations, tests for the Real_x102 and Inco718_Downskin surfaces ended at 60,000.

After the flow conditions were set, a steady-state heat approach was used to determine the surface heat transfer coefficients. Two DC power supplies were turned on which powered the resistance heaters beneath the aluminum test plate. For each test, the heater power was set such that the temperature difference between surface and air was about 15 °C. After the heaters were turned on, the plate was allowed to reach a steady-state temperature. This point was determined to be when plate temperatures had a change of less than 0.1 °C over the preceding 30 min. Once the test plate settled at steady-state temperatures, a final surface temperature image set was taken using the IR camera. Following the test IR acquisition, either the next Reynolds number case was selected or the shutdown procedure was followed.

At steady-state conditions, the convection coefficients were calculated at each pixel of the infrared camera image using Newton's Law of Cooling, as expressed by Eq. (9).

$$h_{i,j} = \frac{\dot{Q}_{conv}}{A_H(T_{IR,i,j} - T_{in})} \quad (9)$$

In Eq. (9), the rate of energy convected from the surface was determined using the heater power and accounting for losses as shown in Eq. (10).

$$\dot{Q}_{conv} = \sum EI - \dot{Q}_{c,a} - \dot{Q}_L - \dot{Q}_{rad} \quad (10)$$

where EI is the product of the voltage and current into each resistance heater, $\dot{Q}_{c,a}$ is the rate of energy transfer through the acrylic base, \dot{Q}_L is the rate of energy transfer longitudinally along the plate, and \dot{Q}_{rad} is the rate of energy transfer from the test surface by radiation to the surrounding wind tunnel walls.

The thermocouple temperature measurements taken above and below the acrylic test stand were used in Eq. (11) to determine the rate of heat energy conducted vertically down through the stand. This calculation used a first-order approximation of Fourier's Law of heat conduction.

$$\dot{Q}_{cond} = k_a(L_p w_p) \frac{(T_{lower} - T_{upper})}{t_a} \quad (11)$$

The amount of heat conducted longitudinally along the plate was determined using Eq. (12).

$$\dot{Q}_L = -k_{Al}(\bar{t}_{Al} w_p) \frac{dT_{IR}}{dx} \quad (12)$$

The energy transferred due to radiation effects was calculated at every pixel of the surface image using the Stefan–Boltzmann law given by Eq. (13).

$$\dot{Q}_{rad} = \sigma \epsilon (L_p w_p) (T_{IR}^4 - T_{in}^4) \quad (13)$$

To provide a scale of the losses existing in the apparatus, for the largest roughness investigated at $Re = 40,000$, conduction through the acrylic accounts for 9.6% of the heater power, longitudinal conduction through the plate accounts for 6.7% of the heater power, radiation accounts for 10.5% of the heater power. The remainder, 73.2%, enters the fluid through convection.

The average convection coefficient was then determined by averaging all of the local convection coefficients in the unmasked area of the infrared images, as shown in Eq. (14).

$$\bar{h} = \sum h_{i,j} M_{i,j} / \sum M_{i,j} \quad (14)$$

where M is the mask matrix. $M_{i,j}$ equals 1.0 if the pixel is acquired from the test surface and equals 0 otherwise. The test area-averaged Nusselt number was evaluated using Eq. (15).

$$\overline{Nu} = \frac{\bar{h} D_h}{k_f} \quad (15)$$

Friction Factor and Velocity Profile Measurements. One reason for performing flow loss and velocity profile measurements using the aluminum heat transfer plates was to verify the frictional similarity of the surfaces created for this study to the rough surfaces used by McClain et al. [7]. The same surface geometry files were used to create both sets of surfaces. However, as noted in Fig. 5 and Table 2, the subtractive machining approach used for the aluminum heat transfer plates created a visibly different surface texture than was created using the computational models from the study of McClain et al. [7].

Details of the volumetric flowrate and friction factor measurements are presented in Hansen et al. [6]. Summarizing Hansen et al. [6], a pressure transducer is used in the RIFT to measure the static pressure in the flow settling region just after the inlet contraction. Treating the contraction as a Venturi nozzle, the measurement is used to calculate the volumetric flowrate, Q , using Eq. (16).

$$Q = C_0 A_{ts} \sqrt{\frac{2 \Delta P_v}{\rho_{air}}} \quad (16)$$

A second pressure transducer is used to measure the losses through a 27-in. length at the exit of the test section and including the heated test surface. The pressure drop is then used to calculate the Darcy–Weisbach friction factor as shown in Eq. (17).

$$f_{DW} = \frac{2 D_h \Delta P_{ts}}{\rho_{air} \left(\frac{Q}{A_{ts}} \right)^2 L_{ts}} \quad (17)$$

The ambient room pressure is measured by a PX409-26USBH barometer, while the room's temperature and relative humidity are measured by an RH-USB sensor. The atmospheric condition measurements allow for the calculation of the moist-air density, ρ_{air} , and viscosity, μ_{air} . The Reynolds number of the flow was then calculated based on the tunnel's hydraulic diameter using Eq. (18).

$$Re_{D_h} = \frac{\rho_{air} D_h Q}{\mu_{air} A_{ts}} \quad (18)$$

Velocity profiles were acquired using the approach described by McClain et al. [7]. An X-array hot-film probe was placed 0.902 m (35.5 in.) downstream of the start of the roughness, which was 0.445 m downstream of the start of the heated section. The probe was moved through a 29.21 mm (1.15-in.) trace in the wall-normal direction in increments of 0.254 mm (0.01 in.) using a stepper-motor controlled stage. At each measurement y-station, 300,000 samples were acquired simultaneously from each wire at a rate of 50,000 samples/s. A fourth-order polynomial was fit to calibration data and used to determine the instantaneous velocities from each hot-film probe wire voltage. The mean x-component velocities at each y-station were then determined and used to generate the velocity profiles. Full details of the hot-film characterization method may be found in McClain et al. [7]. For this investigation, the velocity profiles were acquired while the surfaces were unheated.

Uncertainty Analysis. The uncertainties associated with the calculations of the convection coefficient and the Nusselt number were determined using the large sample size approach of Coleman and Steele [11], which is an extension of the approach of Klein and McClintock [12]. The uncertainty associated with the friction factor measurements was found using a combination of the method of Coleman and Steele and the Moffat [13] method of uncertainty. Because of the compounded fluid property

Table 3 Measurement uncertainties and devices

Meas.	Device	B_X	R_X
H	Calipers	2.54×10^{-5} m	—
w_p	Calipers	2.54×10^{-5} m	—
L_p	Mill gage	2.54×10^{-5} m	—
t_p, t_d	Micrometer	2.54×10^{-6} m	—
ΔP_v	PX2650-2D5V	5 Pa	$\frac{tS_{\Delta P_v}}{\sqrt{N}}$
ΔP_{is}	PX2650-0.5D5V	1.25 Pa	$\frac{tS_{\Delta P_{is}}}{\sqrt{N}}$
E, I	B&K 9104 PSU	0.2% + 0.05	—
T_{IR}	FLIR SC4000	2 K	$\frac{tS_T}{\sqrt{N}}$
T_{ref}			$\frac{tS_T}{\sqrt{N}}$
T_{lower}	Thermocouple, Thermistor	2 K	$\frac{tS_T}{\sqrt{N}}$
T_{upper}			$\frac{tS_T}{\sqrt{N}}$
T_{in}			$\frac{tS_T}{\sqrt{N}}$

dependencies on the fluid temperature, the perturbation approach of Moffat [13] was more convenient for the friction factor evaluation. All uncertainties were determined using a 95% level of confidence. Table 3 reports the systematic and random uncertainties associated with each of the directly measured quantities.

Inspecting Table 3, the systematic uncertainties of the temperature measurements are significant. However, the in situ calibration scheme described by Eqs. (7) and (8) correlates the systematic uncertainties of all of the temperature measurements. The in situ calibration process significantly reduces the resulting uncertainties in the calculated convection coefficients and Nusselt numbers [11].

Results and Discussion

The results are presented in four sections. In the first section, friction factors and velocity profiles are compared to the measurements made for the ABS plastic surfaces used by McClain et al. [7]. In the second section, the heat transfer measurements are presented. In the third section, the measurements are compared to the performance of internal heat transfer enhancement typically employed in gas turbine cooling passages. Finally, the current data are compared to the measurements of Stimpson et al. [5], which were acquired in the START Lab using DMLS coupons with internal channels.

Friction Comparison and Velocity Profiles. As noted earlier, the heat transfer plates were constructed by machining aluminum plates. While the same geometry file was used to create the surfaces used in this study, differences between the heat transfer plates and the ABS plastic plates used by McClain et al. [7] were observed.

The choice of aluminum for the heat transfer investigation was made to minimize the effect of temperature change along the length of the roughness elements. As noted by McClain et al. [14,15], roughness elements behave as fins on a surface. Because of internal thermal resistance, temperature change along the length of the roughness element affects the apparent fin efficiency of the surfaces. Aluminum was chosen to have a low surface resistance as would be expected for metal surfaces created using DMLS printers. The low thermal conductivity ABS surfaces used for the study of McClain et al. [7] would have exhibited significant temperature change along the length of the roughness elements and would not be expected to replicate the enhancement of additive manufacturing roughness.

Figure 6 presents the resulting friction factors from the current study and from the ABS surfaces of McClain et al. [7] versus the Reynolds number based on the hydraulic diameter. In Fig. 6, the overlapping uncertainty bars for the aluminum heat transfer or “HT” surfaces, and the ABS surfaces demonstrate agreement for the two roughest surfaces in the investigations. However, significant

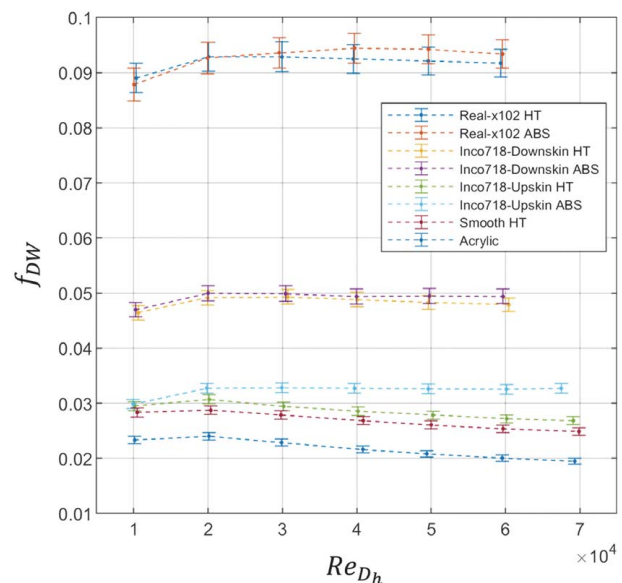


Fig. 6 Comparison of friction factors between ABS surfaces from McClain et al. and aluminum heat transfer surfaces

differences were observed for the Inco718_Upskin surface and the Smooth HT surface, which were compared to the acrylic floor for the hydraulically smooth reference.

The mean velocity profiles measured over the heat transfer surfaces are presented in Fig. 7 for Re_{Dh} values of 30,000 and 60,000. The profiles shown in Fig. 7 reflect similar trends as the velocity profiles presented by McClain et al. [7] for the ABS surfaces.

Figures 6 and 7, when considered with the velocity profiles presented in McClain et al. [7], demonstrate that for Inco718_Downskin and Real_x102 surfaces, the heat transfer plates provide the same flow effects as the ABS surfaces. For the Inco718_Upskin and Smooth surfaces, the machining and painting of the aluminum heat transfer plate produce different flow interactions than the ABS or acrylic surface. The difference between the smooth heat transfer plate and the acrylic smooth reference is surprising, but the flat-black paint has a texture that can be observed and felt by touch.

Convection Measurements. Selected temperature and heat transfer coefficient maps for each surface may be found in Stafford [10]. The resulting average Nusselt number trends for each surface are presented in Fig. 8 over the range of Reynolds numbers investigated. The measured Nusselt numbers are also presented in Tables 4–7. In Fig. 8, the Nusselt number trends are compared to the correlation of Dittus–Boelter as introduced by McAdams [16], which is presented in Eq. (19) for the heating of a fluid.

$$Nu_0 = 0.023 Re_{Dh}^{0.8} Pr^{0.4} \quad (19)$$

Figure 8 demonstrates that the measured Nusselt numbers for each of the rough surfaces increase with Reynolds number and that the Nusselt numbers increase with increasing roughness.

Figure 8 also includes repeatability measurements for the Real_x102 surface. Three measurements of the average Nusselt number were made at $Re_{Dh} = 40,000$, and five measurements of the average Nusselt number were made at $Re_{Dh} = 30,000$ using different heater power levels. The scatter in the repeated measurements is consistent with the calculated uncertainties associated with the Nusselt number measurements.

Figure 9 presents the percentage enhancement. Figure 9 also demonstrates that while there were some hydraulic differences between the smooth heat transfer plate and the acrylic plate used in McClain et al. [7], the convection measurements for the

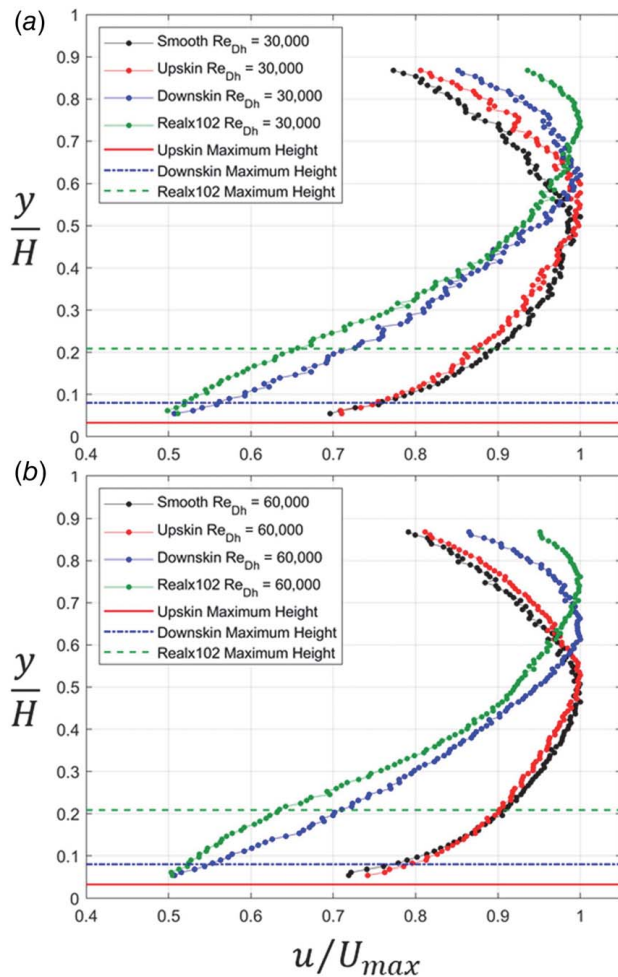


Fig. 7 Velocity profiles measured using X-Array anemometry using aluminum roughness plates: (a) $Re_{Dh} = 30,000$ and (b) $Re_{Dh} = 60,000$

smooth plate agree with Dittus–Boelter equation by 15%. At $Re_{Dh} = 20,000$ and above, the agreement is within 11% and generally improves with increasing Reynolds number.

Figure 9 demonstrates that the enhancement of the rough surfaces is relatively consistent with the Reynolds numbers investigated. For the Inco718_Upskin surface, the enhancement is 17–20%. For the Inco718_Downskin surface, the enhancement is consistently 70–81%, and for the Real_x102 surface, the enhancement is 130–140%.

Tables 4–7 include the calculated Biot number based on the mean thickness of the heated roughness plates. The Biot number is reported to demonstrate that mean wall-normal temperature gradients or temperature changes along the roughness elements should not be significantly affecting the measured convection coefficients.

Comparison to Traditional Enhancement Methods. To investigate the relative performance of additive manufacturing roughness to traditional convection enhancement methods used in internal cooling passages, the increased flow resistance of each surface must also be considered. Ligrani [8] presented a survey of the performance of internal turbine blade convection enhancement methods such as turbulators, dimples, and pin fins, as well as roughness generated in traditional manufacturing methods. In comparing the enhancement methods, Ligrani [8] used two primary parameters: the Reynolds Analogy ratio and the thermal performance ratio, which are defined in Eqs. (20) and (21). The Reynolds

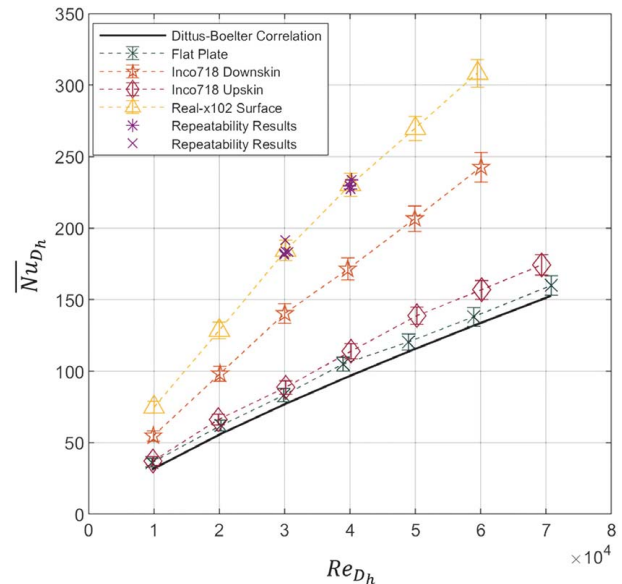


Fig. 8 Measured area-averaged Nusselt numbers

analogy ratio describes the increase in enhancement relative to the increase in friction factor. The global thermal performance parameter, which was introduced by Gee and Webb [17], is used to adjust the enhancement based on providing a comparison to a smooth channel with the same mass flux.

$$RA_r = \frac{(\overline{Nu}/Nu_0)}{(f/f_0)} \quad (20)$$

$$GTP_r = \frac{(\overline{Nu}/Nu_0)}{(f/f_0)^{1/3}} \quad (21)$$

However, the use of single-sided roughness convection measurements complicates the comparison of the roughness measurements to the traditional enhancement methods. Single-sided measurements were used for the current study because of the requirement for IR window access on the opposite wall from the roughness. Because roughness exists on only one wall, the flow migrates toward the smooth wall for the rough surfaces as shown in Fig. 7.

To transform the single-sided roughness measurements and enable a double-sided comparison to the data reported by Ligrani [8], the hydraulic diameter was adjusted, as shown in Eq. (22), based on the location of the maximum velocity at the high-Reynolds number limit presented in Fig. 7(b).

$$D_m = \frac{4A_{adj}}{P_{adj}} = \frac{4(2w_p H \tilde{y})}{2(w_p + 2H \tilde{y})} \quad (22)$$

where $\tilde{y} = y/H$ at the location of maximum streamwise velocity. Essentially, Eq. (22) adjusts the apparent height of the channel to make the location of the maximum velocity a plane of symmetry

Table 4 Summary of convection measurements for smooth aluminum surface

Re	f_{Dw}	\bar{h}	U_h	\overline{Nu}	U_{Nu}	Bi
9714	0.0283	14.73	1.22	35.9	3.0	0.0011
20233	0.0287	25.46	1.56	62.1	3.8	0.0020
29812	0.0279	34.11	1.95	83.2	4.8	0.0026
38919	0.0269	43.03	2.04	104.9	5.0	0.0033
48923	0.0261	49.34	2.34	120.3	5.7	0.0038
58947	0.0254	56.53	2.73	137.9	6.6	0.0044
70761	0.0249	65.55	2.76	159.9	6.7	0.0051

Table 5 Summary of convection measurements for the Inco718_Upskin aluminum surface

Re	f_{DW}	\bar{h}	U_h	\bar{Nu}	U_{Nu}	Bi
9862	0.0295	15.24	1.23	37.2	3.0	0.0012
19887	0.0307	27.17	1.57	66.2	3.8	0.0021
30177	0.0294	36.34	1.90	88.6	4.6	0.0028
40125	0.0285	46.72	2.22	113.9	5.4	0.0036
50207	0.0278	56.93	2.48	138.7	6.0	0.0044
60127	0.0272	64.27	2.72	156.8	6.6	0.0050
69314	0.0268	71.46	2.93	174.3	7.2	0.0055

for the rough-wall flow. The resulting values of \bar{y} and D_m are reported for each surface in Table 1.

Additionally, the friction factors were adjusted using the simulation results reported by McClain et al. [7]. Since the rough wall friction factors were greater than bulk mean friction factors, the simulation results were interrogated to determine the ratio of the rough wall shear to the perimeter average shear. The friction factors were then adjusted using Eq. (23).

$$f = f_{DW} \left(\frac{\tau_R}{\bar{\tau}} \right)_{CFD} \quad (23)$$

The resulting values of the shear ratio are reported in Table 1 for each of the rough surfaces.

Figure 10 presents a comparison of the adjusted Reynolds analogy parameter for convection measurements. In the Reynolds analogy parameter, the reference conditions f_0 and Nu_0 are determined using the Reynolds number determined using the modified hydraulic diameter. The average velocity was not modified in the calculation of the new Reynolds number. The reference friction factor was evaluated using the Colebrook equation presented in Eq. (24) for the hydraulically smooth case, and the reference Nusselt number was determined using the Dittus–Boelter equation presented in Eq. (19).

$$\frac{1}{\sqrt{f_0}} = -2 \log_{10} \left(\frac{2.51}{Re_{D_m} \sqrt{f_0}} \right) \quad (24)$$

Figure 10 shows that the measurements of this investigation collapse when cast in terms of the Reynolds analogy ratio versus the friction factor ratio. The inset of Fig. 10 presents a chart from Ligrani [8] enabling a comparison to different types of internal passage convection enhancement methods. The box in the inset shows the same range used for the presentation of the current data set. Figure 10 demonstrates that, when the current measurements are transformed to reflect roughness over the entire perimeter, the Reynolds analogy ratio trend is comparable to the other methods of passage convective enhancement.

Figure 11 presents the global thermal performance ratios for the surfaces of this study. The inset of Fig. 11 presents a chart from Ligrani [8] reporting the global performance ratios for different types of internal passage convection enhancement methods. The box in the inset indicates the range of global thermal performance values reported in Fig. 11. Comparing the data of the current

Table 6 Summary of convection measurements for the Inco718_Downskin aluminum surface

Re	f_{DW}	\bar{h}	U_h	\bar{Nu}	U_{Nu}	Bi
9923	0.0464	22.45	1.47	54.7	3.6	0.0017
20125	0.0491	40.34	2.19	98.2	5.3	0.0031
30022	0.0493	57.63	2.78	140.4	6.8	0.0045
39645	0.0488	70.32	3.21	171.4	7.8	0.0055
49919	0.0483	84.69	3.66	206.7	8.9	0.0066
60052	0.0479	99.67	4.30	242.7	10.5	0.0077

Table 7 Summary of convection measurements for the Real_x102 aluminum surface

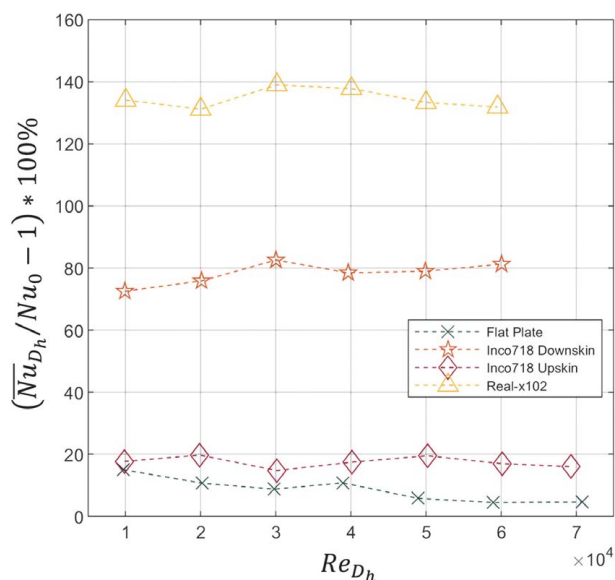
Re	f_{DW}	\bar{h}	U_h	\bar{Nu}	U_{Nu}	Bi
10033	0.0890	30.69	1.72	74.9	4.2	0.0024
20017	0.0929	52.65	2.42	128.5	5.9	0.0041
30151	0.0928	75.66	2.95	184.4	7.2	0.0059
40069	0.0925	94.50	3.30	230.3	8.1	0.0073
50002	0.0921	110.63	3.51	269.8	8.6	0.0086
59523	0.0917	126.42	3.94	308.2	9.6	0.0098

study to the data compiled by Ligrani [8], many passage enhancement methods provide greater global thermal performance than the additively manufactured roughness investigated in this study. For the AM roughness investigated, the maximum global thermal performance is on the order of 1.4, while the data compiled by Ligrani [8] reach as high as 2.25 for swirl chambers, dimples, and ribs. The comparison of Fig. 11 demonstrates that AM surfaces will enhance the heat transfer in internal passages; however, additional enhancements mechanisms may still be required in the additive manufacturing geometries to reach global thermal performance values achieved by traditional convection enhancement methods.

Comparison to Data From Stimpson et al. The adjusted convection enhancements were also compared to the measurements of Stimpson et al. [4] for engine-scale additively manufactured passages created and tested in the START Lab at Pennsylvania State University. Data covering the range of enhancement ratios (Nu/Nu_0) from Stimpson et al. [4] are included in Fig. 10 for the Reynolds analogy comparison. Figure 10 demonstrates that the engine-scale data follow a similar trend as the measurements presented in this study for scaled passages and are scattered about the trend observed for the scaled passages.

The collapsing of the Reynolds analogy data suggests a correlation approach for the scaled passage measurements. That is, the collapse of the scaled passage Reynolds analogy ratios as a function of friction factor ratio may be expressed as shown in Eq. (25) as a generic function or a power-law function.

$$\frac{(\bar{Nu}/Nu_0)}{(f/f_0)} = F(f/f_0) \approx a(f/f_0)^b \quad (25)$$

**Fig. 9 Percentage enhancement above Dittus–Boelter prediction for smooth surfaces**

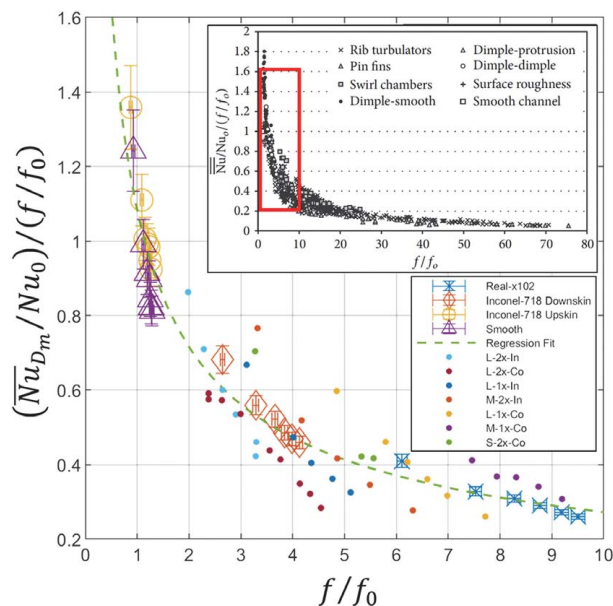


Fig. 10 Reynolds analogy comparison for the scaled additively manufactured roughness and including data from Stimpson et al. [4]. Inset reproduced from [8] Creative Commons Attribution 3.0 Unported (CC BY 3.0).

Figure 10 includes a best-fit regression curve based on the scaled passage convection measurements of this study. The resulting power-law parameters were determined to be $a=1.08$ and $b=-0.599$. Multiplying Eq. (25) by the friction factor ratio results in a Nusselt correlation as shown in Eq. (26).

$$\overline{Nu}/Nu_0 = a(f/f_0)^{b+1} \quad (26)$$

The correlation of Eq. (26) follows a Norris [18] style approach, but Eq. (26) results in a different exponent for the friction ratio ($b+1=0.401$ versus $n=0.68Pr^{0.215}=0.633$ for the correlation provided by Norris [18]).

Figure 12 presents a comparison of the predictions for the scaled passage enhancement ratios of this study and for the measurements of Stimpson et al. [4] as a function of $(f/f_0)^{0.401}$. Figure 12

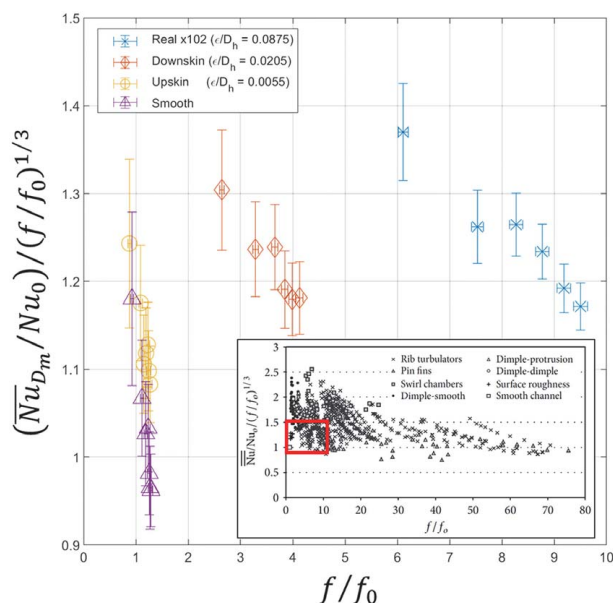


Fig. 11 Thermal performance comparison for the additively manufactured roughness. Inset reproduced from [8] Creative Commons Attribution 3.0 Unported (CC BY 3.0).

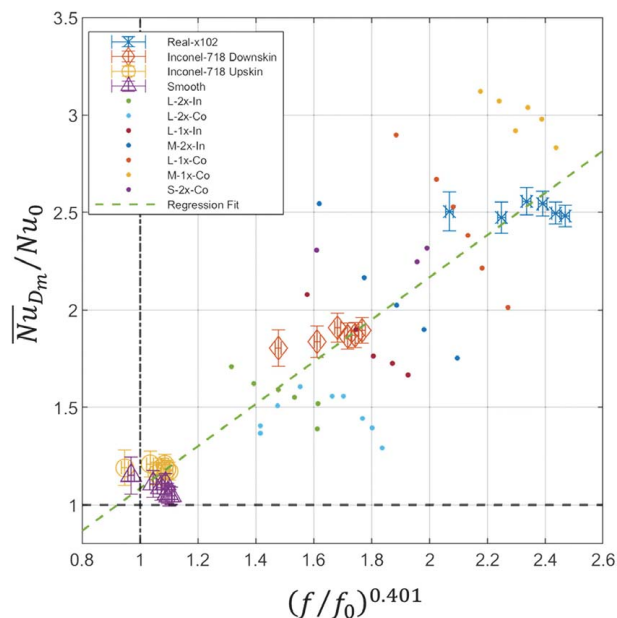


Fig. 12 Resulting Reynolds analogy correlation and comparison to data from Stimpson et al. [4].

demonstrates that the modified enhancement ratios measured for scaled passages with AM roughness capture the trend of the Stimpson et al. [4] measurements. However, the agreement with the scaled passage data is $\pm 10\%$, while the agreement with the data from Stimpson et al. [4] is $\pm 50\%$.

The scaled passage convection measurements in the RIFT were designed to isolate the nature of additively manufactured roughness. Figure 12 indicates that the overall trend of friction enhancement and convection enhancement caused by AM roughness is captured by the RIFT measurements. However, physics not captured in the scaled passage measurements are clearly affecting the engine-scale measurements. Important phenomena not included in the RIFT measurements that are present in the engine-scale tests are (1) compressibility effects and (2) long-wavelength effects caused by the additive manufacturing process such as concentricity, circularity, and total runout [2,19].

The data reduction equations used by Stimpson et al. are based on the incompressible modified Bernoulli equation and constant specific heat energy equation. Stimpson [20] presents an investigation of the friction factor measurements considering compressible flow behavior in the channels and found that compressibility effects should only be important at the highest flowrates investigated. However, the heated coupon cases at the high Reynolds numbers are experiencing a more complicated Fanno-Rayleigh situation that may not be captured appropriately using the data reduction equations of Stimpson et al. [4] or Stimpson [20].

Inspecting Fig. 12, two features may point to a correction for real, engine-scaled passages. In Fig. 12, the scaled AM measurements in the RIFT and the correlation run through the middle of the engine-scale data. However, the RIFT enhancement ratios are essentially constant, while engine-scale measurements decrease with increasing friction factor ratio. Revisiting Stimpson et al. [4], the engine-scale measurements are in the lower half of Reynolds numbers investigated in the RIFT. The measurements of Stimpson et al. [4] also appear to cross the correlation as the Reynolds number increases. The fact that the engine-scale data from the START Lab cross the correlation as the Reynolds number increases suggest that a velocity-based or Reynolds-based feature is affecting the measurements in a way that is not present in the RIFT data. The fact that the RIFT data are also in the “fully-rough” regime where the friction factor is no longer changing with Reynolds number, while the engine-scale tests of Stimpson et al. appear to still be in the “transitionally rough” regime. In any case, explaining the differences

between the Stimpson et al. [4] data and the scaled RIFT data is an active area of research.

Conclusion

Convection measurements were made in a scaled passage using rough surfaces with characteristics of additively manufactured roughness. Steady-state convection measurements were made using machined aluminum surfaces to minimize the effects of temperature change along the length of the roughness elements. The primary findings of the investigation are as follows:

- (1) Frictional differences between the aluminum heat transfer roughness plates and the ABS plates created for the investigation were negligible for the two surfaces with larger roughness. For the surface with the smallest roughness characteristics and for the smooth heat transfer surface, fluid friction differences were more significant.
- (2) The percentage enhancements for the scaled surfaces relative to the Dittus–Boelter correlation were essentially constant for cases investigated.
- (3) The scaled AM passage measurements were modified for comparison to the data from Ligrani [8]. Following modification to represent channels with roughness around the perimeter, the AM roughness behaves similar to traditional internal convective enhancement devices based on the Reynolds analogy parameter. However, when compared using the global thermal performance ratio, the AM surfaces did not perform as well as swirl chambers, dimples, and ribs.
- (4) The Reynolds analogy ratio collapses the scaled AM roughness convection measurements when reported versus the friction enhancement ratio suggesting a Norris [18] style correlation. A correlation was provided and produces agreement levels within $\pm 10\%$ of the measurements in the RIFT.
- (5) The scaled AM passage enhancement ratios and resulting correlation are in line with the engine-scale test data from Stimpson et al. [4]. However, the scatter about the correlation is $\pm 50\%$ for the engine-scale measurements of Stimpson et al. [4].

Acknowledgment

This material is based upon work supported by the Department of Energy under Award Number(s) DE-FE0001730. Mr. Ashley Orr's efforts in machining the aluminum heat transfer plates are greatly appreciated.

Disclaimer

This report was prepared as an account of work sponsored by an agency of the United States Government. Neither the United States Government nor any agency thereof, nor any of their employees, makes any warranty, express or implied, or assumes any legal liability or responsibility for the accuracy, completeness, or usefulness of any information, apparatus, product, or process disclosed or represents that its use would not infringe privately owned rights. Reference herein to any specific commercial product, process, or service by trade name, trademark, manufacturer, or otherwise does not necessarily constitute or imply its endorsement, recommendation, or favoring by the United States Government or any agency thereof. The views and opinions of authors expressed herein do not necessarily state or reflect those of the United States Government or any agency thereof.

Conflict of Interest

There are no conflicts of interest.

Data Availability Statement

The datasets generated and supporting the findings of this article are obtainable from the corresponding author upon reasonable

request. The authors attest that all data for this study are included in the paper. Data provided by a third party are listed in Acknowledgment.

Nomenclature

h	= convection coefficient
u	= the velocity component in the flow direction
y	= location in the wall-normal location in the fluid domain
H	= the channel height 36.07 mm (1.42 in.)
Q	= volumetric flowrate
Y	= wall-normal direction and ordinate of a specific surface location
\dot{Q}	= heat rate
\bar{Y}	= mean surface location
Y'	= surface elevation relative to the mean elevation
A_H	= the heated platform area (top-view projected area)
A_{ts}	= test section cross-sectional area = 8200 mm ²
B_X	= systematic uncertainty of the X measurement
C_0	= nozzle or Venturi discharge coefficient
D_h	= the RIFT hydraulic diameter = 62.3 mm (2.45 in.)
D_m	= the modified hydraulic diameter adjusting for the velocity profile shift caused by roughness on one wall of the RIFT
f_{DW}	= Darcy–Weisbach friction factor
k_{Al}	= the thermal conductivity of aluminum 6061
$k_{s,FS}$	= the predicted equivalent sand-grain roughness height using Flack and Schultz (2010) correlation
$k_{s,ST}$	= the predicted equivalent sand-grain roughness height using Stimpson and Thole correlation
t_a	= thickness of the acrylic base
\bar{t}_p	= average thickness of the heated test plate 12.7 mm (0.5 in.)
w_p	= width of the heated test plate 228.6 mm (9 in.)
L_p	= length of the heated test plate 457.2 mm (18 in.)
L_s	= length of the flow settling region from the nozzle exit to the first pressure tap
L_{ts}	= length of the RIFT pressure-drop metered section = 685.8 mm (27.0 in.)
N_p	= number of points in surface point cloud
R_a	= the arithmetic mean roughness
R_{PV}	= the peak-to-valley roughness
R_q	= the root-mean-square roughness
R_X	= random uncertainty of the X measurement
T_{cal}	= instrument raw temperature during calibration
T_{in}	= temperature of the air at the RIFT inlet
T_{IR}	= unmasked infrared temperature measurement
T_{lower}	= temperature of thermocouples attached to the bottom of the acrylic base
T_m	= instrument raw temperature during measurement
T_{ref}	= calibration reference temperature
T_{run}	= calibrated temperature during measurement
$T_{um,cal}$	= temperature of unmasked infrared measurement region during calibration
T_{upper}	= temperature of thermocouples in recessed channels machined in acrylic base and just below heaters
U_{mean}	= average flow speed over the tunnel cross section
ΔP_v	= gage pressure at the nozzle or Venturi exit
ΔP_{ts}	= pressure drop from first to last pressure taps
Bi	= Biot number = $h\bar{t}_p/k_{Al}$
Re_{Dh}	= Reynolds number based on the hydraulic diameter, $Re_{Dh} = \rho U_{mean} D_h / \mu$
Skw	= roughness height relative skewness distribution

Greek Symbols

μ_{air}	= the molecular viscosity of air
ρ_{air}	= the density of air
$\bar{\tau}$	= the perimeter averaged shear
τ_R	= the shear on the rough perimeter of the channel

Subscripts and Accents

m = measured quantity

(\cdot) = time-averaged quantity

References

- [1] Han, J.-C., and Chen, H.-C., 2006, "Turbine Blade Internal Cooling Passages with Rib Turbulators," *J. Propul. Power*, **22**(2), pp. 226–248.
- [2] Snyder, J. C., Stimpson, C. K., Thole, K. A., and Mongillo, D. J., 2015, "Build Direction Effects on Microchannel Tolerance and Surface Roughness," *ASME J. Mech. Des.*, **137**(11), p. 111411.
- [3] Kirsch, K. L., and Thole, K. A., 2017, "Heat Transfer and Pressure Loss Measurements in Additively Manufactured Wavy Microchannels," *ASME J. Turbomach.*, **139**(1), p. 011007.
- [4] Stimpson, C. K., Snyder, J. C., Thole, K. A., and Mongillo, D., 2016, "Roughness Effects on Flow and Heat Transfer for Additively Manufactured Channels," *ASME J. Turbomach.*, **138**(5), p. 051008.
- [5] Stimpson, C. K., Snyder, J. C., Thole, K. A., and Mongillo, D., 2017, "Scaling Roughness Effects on Pressure Loss and Heat Transfer of Additively Manufactured Channels," *ASME J. Turbomach.*, **139**(2), p. 021003.
- [6] Hanson, D. R., McClain, S. T., Snyder, J. C., Kunz, R. F., and Thole, K. A., 2019, "Flow in a Scaled Turbine Coolant Channel With Roughness Due to Additive Manufacturing," Volume 5B: Heat Transfer, American Society of Mechanical Engineers, Phoenix, AZ, p. V05BT21A004, Paper No. GT2019-90931.
- [7] McClain, S. T., Hanson, D. R., Cinnamon, E., Snyder, J. C., Kunz, R. F., and Thole, K. A., 2020, "Flow in a Simulated Turbine Blade Cooling Channel with Spatially Varying Roughness Caused by Additive Manufacturing Orientation," ASME Turbo Expo 2020, Turbomachinery Technical Conference and Exposition, Virtual Conference, Sept. 21–25, Paper No. GT2020-16069.
- [8] Ligrani, P., 2013, "Heat Transfer Augmentation Technologies for Internal Cooling of Turbine Components of Gas Turbine Engines," *Int. J. Rotating Mach.*, **2013**, pp. 1–32.
- [9] Flack, K. A., and Schultz, M. P., 2010, "Review of Hydraulic Roughness Scales in the Fully Rough Regime," *ASME J. Fluid. Eng.*, **132**(4), p. 041203.
- [10] Stafford, G. J., 2020, "Convection Measurements in Scale Models of Additively Manufactured Turbine Blade Cooling Passages," M.S. thesis, Baylor University, Waco, TX.
- [11] Coleman, H., and Steele, W. G., 1999, *Experimentation and Uncertainty Analysis for Engineers*, Wiley, New York.
- [12] Kline, S. J., and McClintock, F. A., 1953, "Describing Uncertainties in Single-Sample Experiments," *Mech. Eng.*, **75**(1), pp. 3–8.
- [13] Moffat, R., 1988, "Describing Uncertainties in Experimental Results," *Exp. Therm. Fluid Sci.*, pp. 3–17.
- [14] Mart, S. R., McClain, S. T., and Wright, L. M., 2012, "Turbulent Convection From Deterministic Roughness Distributions with Varying Thermal Conductivities," *ASME J. Turbomach.*, **134**(5), p. 051030.
- [15] McClain, S. T., Vargas, M., Kreeger, R. E., and Tsao, J.-C., 2007, "Heat Transfer From Protuberances," *J. Thermophys. Heat Transfer*, **21**(2), pp. 337–345.
- [16] McAdams, W. H., 1942, *Heat Transmission*, 2nd ed., McGraw-Hill, New York.
- [17] Gee, D. L., and Webb, R. L., 1980, "Forced Convection Heat Transfer in Helically Rib-Roughened Tubes," *Int. J. Heat Mass Transfer*, **23**(8), pp. 1127–1136.
- [18] Norris, R. H., 1971, "Some Simple Approximate Heat Transfer Correlations for Turbulent Flow in Ducts With Surface Roughness," *Augmentation of Convection Heat and Mass Transfer*, American Society of Mechanical Engineers, New York.
- [19] Wildgoose, A. J., Thole, K. A., Sanders, P., and Wang, L., 2020, "Impact of Additive Manufacturing on Internal Cooling Channels with Varying Diameters and Build Directions," ASME Turbo Expo 2020, Turbomachinery Technical Conference and Exposition, Virtual Conference, Sept. 21–25, Paper No. GT2020-15049.
- [20] Stimpson, C. K., 2017, "Cooling Performance of Additively Manufactured Microchannels and Film Cooling Holes," Ph.D. dissertation, The Pennsylvania State University, State College, PA.